COMMUNICATION

Engineering Au/MnO₂ hierarchical nanoarchitectures for ethanol electrochemical valorization

Lorenzo Bigiani,[a] Teresa Andreu,[bc] Chiara Maccato,*[a] Ettore Fois,[d]
Alberto Gasparotto,[a] Cinzia Sada,[e] Gloria Tabacchi,*[d] Dileep Krishnan,[f]
Johan Verbeeck,[f] Juan Ramón Morante[bc] and Davide Barreca[g]

The design of eco-friendly electrocatalysts for ethanol valorization is an open challenge towards sustainable hydrogen production. Herein we present an original fabrication route to effective electrocatalysts for ethanol oxidation reaction (EOR). Herein, hierarchical MnO₂ nanostructures are grown on high-area nickel foam scaffolds by a plasma-assisted strategy and functionalized with low amounts of optimally dispersed Au nanoparticles. This strategy leads to catalysts with unique morphology, designed to enhance reactant-surface contacts and maximize active sites utilization. The developed nanoarchitectures show superior performances for ethanol oxidation in alkaline media. We reveal that Au decoration boosts MnO₂ catalytic activity by inducing pre-dissociation and pre-oxidation of the adsorbed ethanol molecules. These evidences candidate our strategy as an effective route in the development of green electrocatalysts for efficient electrical-to-chemical energy conversion.

The exploitation of clean and renewable energy resources is a strategic key to underpin the global demand of social/industrial developments.[1-6] In this context, biomass-derived ethanol (EtOH) stands as a promising fuel thanks to its high energy density (29.7 MJ×kg⁻¹) low toxicity and easy storage, that have stimulated its valorization in direct ethanol fuel cells (DEFCs) for portable/transportation electronics.[7-15] In particular, DEFCs have attracted attention for the production of hydrogen, a clean and sustainable energy vector,[1, 2, 4, 16-21] especially with electricity from renewable sources.[5] To date, the most effective DEFC anodic catalysts are based on noble metals (especially Pt),[6, 8, 12, 22] but their high cost, supply shortage and limited life cycle[4, 14, 16, 23, 24] have triggered the research on alternative materials.[22, 25] In this context, various works have focused on composites based on metal nanoparticles (MNPs) and metal oxides,[5, 6, 10, 11, 13, 22-24] the latter acting simultaneously as co-catalysts and supports to avoid MNP agglomeration.[17, 25-29]

Among cost-effective and eco-friendly oxides, manganese ones,[3, 27, 30-35] and, in particular, MnO₂, offering a rich polymorphism and a good electrochemical behavior,[2, 8, 16, 19, 29] have been used in electrocatalysts for oxygen evolution (OER)[17, 27, 28, 32, 34, 36] and reduction reactions (ORR),[3, 29, 35, 37, 38] as well as in organics electrooxidation.[8-10, 19] So far, most electrocatalysts have been prepared through powders immobilization on substrates using slurries with additives/binders,[2-4, 7-9, 22, 29, 31, 34, 35, 38] compromising the resulting performances.[4, 22] These issues can be tackled using MnO₂-based electrocatalysts as supported systems/thin films,[10, 17-19, 28, 30, 32, 33, 36] whose performances are critically affected by the adopted fabrication route[2, 25, 31] To further boost catalytic activity, valuable alternatives are offered by high area scaffolds-supported 3D hierarchical architectures,[3, 32, 38] providing fast pathways for ion/charge carrier diffusion,[11, 19, 22] and by the functionalization with MNPs, since the presence of tunnels in MnO₂ structure can also strengthen interactions with supported metals.[3, 9, 10] Among the latter, gold has offered appreciable performance improvements in combination with MnO₂.[17, 27-29] These successes prompt to attain a deeper understanding of Au NPs role, aimed at further extending the applications of manganese oxide electrocatalysts. For example, while β-MnO₂ - the most abundant and stable MnO₂ polymorph[35] - has been used in OER[3, 31] and ORR,[35] to the best of our knowledge it was never tested for EOR in alkaline media.

Herein, we propose 3D MnO₂ hierarchical nanoarchitectures functionalized with Au NPs as new electrocatalysts for the alkaline ethanol oxidation reaction (EOR). For the first time, electrocatalyst preparation is performed by plasma assisted-chemical vapor deposition (PA-CVD) of β-MnO₂, followed by functionalization with gold NPs *via* radio frequency (RF)-sputtering (Fig. 1a). Commercial Ni

[a.] Department of Chemical Sciences, Padova University and INSTM, 35131 Padova, Italy. E-mail: chiara.maccato@unipd.it
[b.] IREC, Catalonia Institute for Energy Research, 08930 Sant Adrià de Besòs, Barcelona, Catalonia, Spain
[c.] Universitat de Barcelona (UB), 08028 Barcelona, Spain
[d.] Department of Science and High Technology, Insubria University and INSTM, 22100 Como, Italy. E-mail: gloria.tabacchi@uninsubria.it
[e.] Department of Physics and Astronomy, Padova University and INSTM, 35131 Padova, Italy
[f.] EMAT and NANOlab Center of Excellence, University of Antwerp, 2020 Antwerpen, Belgium
[g.] CNR-ICMATE and INSTM, Department of Chemical Sciences, Padova University, 35131 Padova, Italy
† Electronic Supplementary Information (ESI) available. See DOI: 10.1039/x0xx00000x
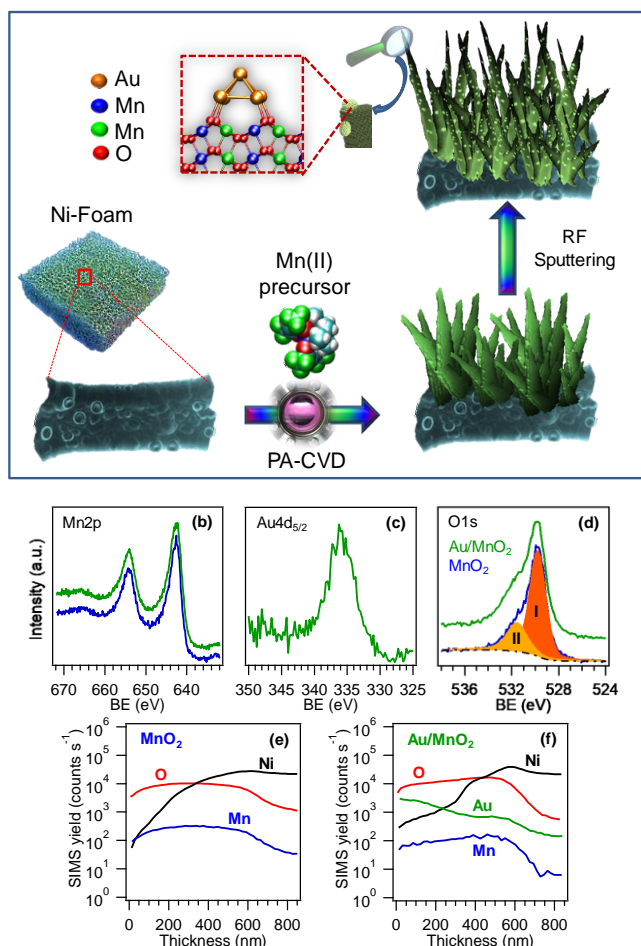
Fig. 1 (a) Schematics of the strategy used for the fabrication of Au-MnO$_2$ nanosystems on Ni foam *via* PA-CVD and their functionalization with Au NPs by RF-sputtering (square inset: Au-MnO$_2$ interface structure). Surface Mn2p (b), Au4d$_{5/2}$ (c), and O1s (d) photoelectron peaks for the target specimens. SIMS depth profiles for MnO$_2$ (e) and Au/MnO$_2$ (f) samples.

foams (NFs),[1, 4] featuring a high electric conductivity and a desirable open-pore structure,[19] are adopted as scaffolds. The resulting materials show electrocatalytic performances comparing favourably with the best oxide-based catalysts known to date. Indeed, MNP functionalization produces a substantial enhancement of the EOR activity: in particular, the Au/MnO$_2$ sample showed a current density of 63 mA/cm^2 at 1.6 V *vs.* the reversible hydrogen electrode (RHE; +43% with respect to bare MnO$_2$) and a voltage needed to reach 10 mA/cm^2 30 mV lower than MnO$_2$. Density functional theory (DFT) calculations reveal that gold NPs increase the catalyst electron acceptor properties and poise ethanol to the target EOR process.

The system surface composition and element valence states were probed by X-ray photoelectron spectroscopy (XPS). Survey spectra (Fig. S1a†) were dominated by the presence of Mn and O photoelectron and Auger signals, beside the C1s signal due to air exposure, and clearly showed the presence of gold peaks after functionalization by RF-sputtering. The occurrence of MnO$_2$ was confirmed by the analysis of Mn2p signal [Fig. 1b; Mn2p$_{3/2}$ and Mn2p$_{1/2}$ binding energy (BE) = 642.5 eV and 654.1 eV, splitting = 11.6 eV][3, 8, 34, 39] and by the Mn3s multiplet splitting separation (4.7 eV; Fig. S1b†).[36-38, 40] The Au4d$_{5/2}$ peak

confirmed the occurrence of the sole Au(0) (Fig. 1c; BE(Au4d$_{5/2}$) = 335.2 eV], although the recorded BE value was slightly higher (≈ 0.2 eV) than the typical ones for metallic gold.[17] This phenomenon, in line with previous literature findings,[41] highlighted the occurrence of an Au→MnO$_2$ electron transfer, as also indicated by the results of theoretical calculations (see below). For Au/MnO$_2$, the gold molar fraction (see ESI†) was determined to be X_{Au} = 10 %. The O1s photopeak (Fig. 1d) resulted from the concurrence of two bands at BE = 529.8 (**I**) and 531.6 eV (**II**) (≈27 % and 37 % of the total O signal, for MnO$_2$ and Au/MnO$_2$, respectively), assigned respectively to O-Mn bonds and to -OH groups/adsorbed oxygen species.[1, 3, 9, 14, 19, 38, 41] Secondary ion mass spectrometry (SIMS) depth profiling (Fig. 1e and f) evidenced a negligible carbon contamination (< 25 ppm) and an almost parallel trend of Mn and O ionic yields throughout the sampled thickness, supporting the uniform formation of MnO$_2$ in the entire deposit. In the case of Au/MnO$_2$ (Fig. 1f), gold resulted predominantly located in the outermost system region, and its signal underwent a slight decrease at higher depths. The appreciable Au-MnO$_2$ intermixing was
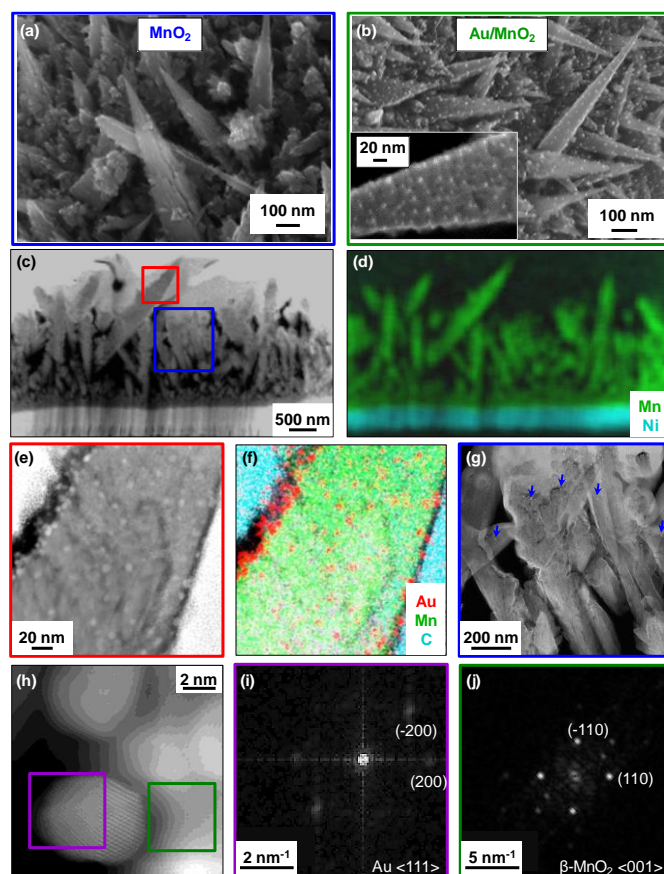

Fig. 2 SEM images of MnO$_2$ (a) and Au/MnO$_2$ (b) specimens. TEM characterization of the Au/MnO$_2$ sample. (c) HAADF-STEM overview image, and (d) corresponding EDXS chemical map showing NiKα and MnKα signals from NF substrate and MnO$_2$ nanoaggregates. (e) Higher magnification HAADF-STEM image of the red-squared area in (c), and (f) corresponding EDXS map. The C signal is from glue used in sample preparation. (g) HAADF-STEM micrograph of the blue-squared area in (c). Arrows mark Au NPs located at the top of MnO$_2$ aggregates. (h) HR-STEM image of the interfacial Au/MnO$_2$ region. (i,j) SAED patterns from the violet and green-squared regions in (h), corresponding to Au and β-MnO$_2$, respectively.

2 | *J. Mater. Chem. A*, 2020, **00**, 1-3

This journal is © The Royal Society of Chemistry 20xx

ascribed to the synergy between MnO_2 porous structure and the typical RF-sputtering infiltration power. These characteristics were also responsible for the tailing of signals into the NF substrates, resulting in broad deposit-NF interfaces.

Fig. 2a and S2† report scanning electron microscopy (SEM) micrographs for bare MnO_2 and Au/MnO_2 specimens. The images revealed a homogeneous coverage of the whole NF skeleton, without any significant alteration of its original structure (see Fig. S2a†), by quasi-1D MnO_2 nanoaggregates (mean length and diameter = 200÷1200 nm and 100 nm, respectively), whose assembly resulted in a 3D hierarchical architecture. Such high-area open structures are extremely advantageous for electrocatalytic end-uses,[2, 3, 6, 10, 11, 13, 31] since they can ease reactant transport into the interior active sites,[7, 23] provide enough room for the diffusion of both electrolyte and reactant molecules[4, 22, 38] and maximize the subsequent gold loading.[19] Functionalization by RF-sputtering (Fig. 2b) yielded almost spherical gold NPs (mean diameter ≈ 6 nm), dispersed over MnO_2 nanostructures (Fig. 2b, inset). Imaging in different regions indicated the lateral homogeneity of Au/MnO_2 nanocomposites.

In order to investigate the system nanoscale structure, high angle annular dark field-scanning transmission electron microscopy (HAADF-STEM), high resolution (HR)-TEM, and energy dispersive X-ray spectroscopy (EDXS) analyses were carried out on an Au/MnO_2 specimen. HAADF-STEM and EDXS data in Fig. 2c and d highlighted the assembly of quasi-1D hierarchical structures with pointed tips outgrowing from the underlying NF substrate, in line with FE-SEM results (Fig. 2a, b and S2†). A uniform dispersion of low-sized Au NPs, preferentially located on the top of quasi-1D MnO_2 structures, was clearly evidenced (Fig. 2e and g). These indications are in line with those provided by high magnification EDXS elemental maps and line-scan profiles across the Au/MnO_2 interface (Fig. S3†). Selected area electron diffraction (SAED) indicated the presence of polycrystalline tetragonal β-MnO_2 as the sole Mn(IV) oxide polymorph, and of face centered cubic (fcc) Au (Fig. 2i and j, S4† and S5†). Additional HR imaging (Fig. 2h and S6†) revealed an intimate Au/MnO_2 interfacial contact, a result of crucial importance for the exploitation of synergistic metal-oxide effects in electrocatalytic applications.

The catalytic activity of the target systems towards ethanol electrooxidation was subsequently evaluated in an alkaline medium (0.5 M KOH, 0.5 M ethanol; Fig. 3a). Fig. 3b shows the EOR performance of Au/MnO_2 specimen compared with bare MnO_2, both supported on NFs, and bare Ni foam. Onset potential (i.e., the potential required to reach a 0.1 mA/cm^2 current density) and $E_{j=10}$ (voltage needed to reach 10 mA/cm^2)[16] (see Table S1†) followed the trend: Ni foam = Au/Ni foam > MnO_2 > Au/MnO_2. These data clearly demonstrate the beneficial role of MnO_2 and Au/MnO_2 on the overall material performances. Furthermore, to the best of our knowledge, the activities of MnO_2 and Au/MnO_2, expressed in terms of current density at fixed potential and $E_{j=10}$ (2nd and 3rd column, Table S2†), compare favourably with the best performing oxide-based materials reported in the literature so far,[5-7, 10, 11, 13, 15, 24, 42] in particular for Au/MnO_2. Since gold NPs onto Ni did not provide
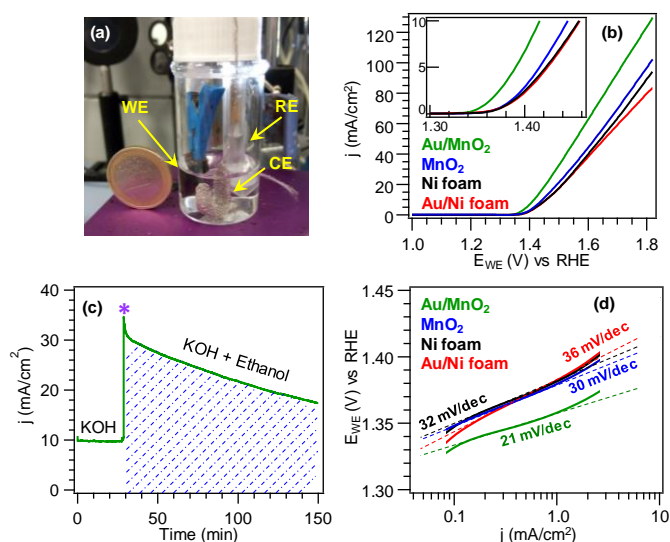
Fig. 3 (a) Digital photograph of the cell used for electrochemical tests. (b) Linear sweep voltammetry (LSV) curves obtained in 0.5 M KOH + 0.5 M EtOH. Data for bare NFs and Au/NFs are reported for comparison. (c) Chronoamperometry data for the Au/MnO_2 specimen obtained applying a constant potential of 1.5 V vs. RHE. Ethanol introduction is marked by *. (d) Tafel plots and pertaining slope values for the different specimens, corresponding to LSV curves of Fig. 3b.

higher current density with respect to bare Ni foam (compare red and black curves in Figure 3b), the observed enhancement could be related to a synergistic interaction between MnO_2 and Au NPs, further elucidated by theoretical calculations (see below).

Further information was gained by chronoamperometry (CA) data (Fig. 3c) recorded in KOH (first 30 min) and ethanol/KOH solutions (subsequent 120 min). In KOH the current density was almost constant, highlighting a good material stability. After EtOH introduction j values increased and subsequently declined, confirming thus the occurrence of ethanol consumption and a higher catalytic activity in EOR than OER (Fig. S7†). The analysis of Tafel slope values (Fig. 3d) yielded the following trend: Au/Ni foam > Ni foam > MnO_2 > Au/MnO_2, revealing that the latter was the best performing system. These results confirm that: i) gold NPs did not boost the reaction without MnO_2, ii) MnO_2 deposited onto Ni foam allowed a slight catalytic activity improvement in comparison to bare Ni foam, iii) Au/MnO_2 resulted appreciably more active than MnO_2 and Ni foam. These observations pinpoint the key role of MnO_2-Au interface in enhancing electrocatalytic performances, and prompted its theoretical investigation.

DFT calculations were performed on a slab model of MnO_2(101) surfaces with on-top Au nanoparticles, computing the structural and electronic properties of bare MnO_2 (Fig. 4a) and Au-decorated MnO_2 (Fig. 4b; ESI†, § S4 and Fig. S8†). Remarkably, Au is in close contact with MnO_2 surface oxygens (mean Au–O_{Au} distance: 2.16 Å), in line with the atomistic-level behaviour for Au on Mn oxide surfaces.[43] Such a strong metal-oxide interaction significantly perturbs MnO_2 electronic structure, resulting in an energy gap decrease by 0.13 eV and a Fermi level (E_f) shift towards occupied states (Fig. 4e). In addition, whereas the density of states (DOS) for bare MnO_2 is
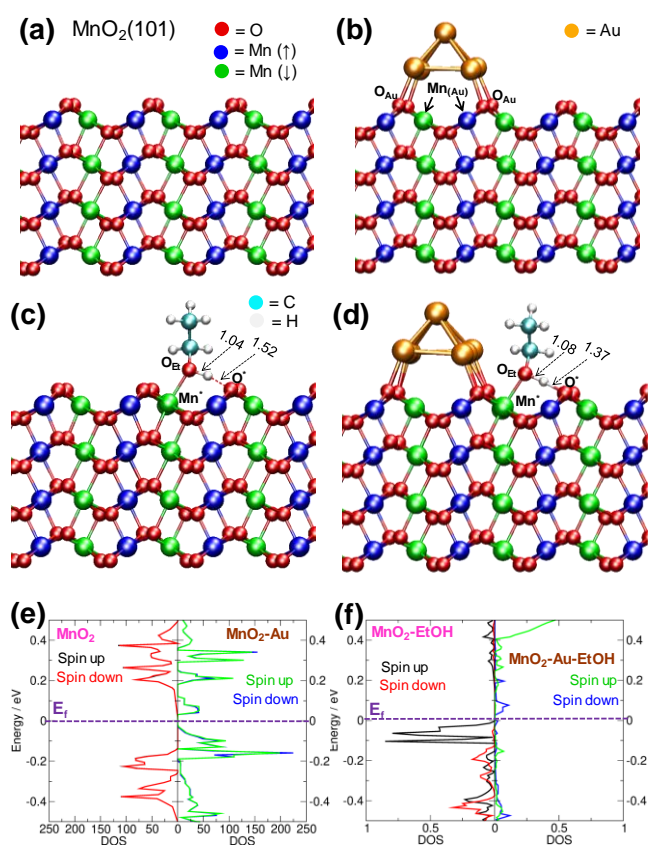
This journal is © The Royal Society of Chemistry 20xx

J. Mater. Chem. A, 2013, **00**, 1-3 | **3**

Please do not adjust margins

Fig. 4 Graphical representation of: a) bare $MnO_2(101)$ slab; b) Au-decorated MnO_2; EtOH adsorbed on MnO_2 (c) and Au/MnO_2 (d) surfaces. Atom colors: O= red; Mn(spin up) = blue; Mn(spin down) = green; Au = orange; C = cyan; H = white. Reported interatomic distances are in Å. e) Density of states (DOS) for bare MnO_2 (left) and Au/MnO_2 (right). f) DOS projected on EtOH O_{2p}-states for EtOH adsorbed on bare MnO_2 (left) and Au/MnO_2 (right).

nearly zero above E_f, the Au/MnO_2 surface exhibits a substantially higher DOS (Fig. 4e) and, hence, a higher number of low-energy empty states ready to accept electron density from EtOH.

Additionally, in accordance with XPS results, an $Au{\rightarrow}MnO_2$ electron transfer takes place (§ S5, ESI†). Charge donation from Au is not inherently a surface property, as it also occurs from Au dopant interstitial atoms in MnO_2.[41] However, the modifications exerted by Au on the electronic structure of the catalyst surface are more profound and deeply affect ethanol adsorption. As depicted in Fig. 4c, EtOH strongly binds to clean MnO_2 (binding energy = 26.7 kcal/mol): it is coordinated to a Mn site (d(Mn*−O_{Et}) = 2.00 Å), and hydrogen bonded to a close surface oxygen (d(O_{surf}−H) = 1.52 Å). On Au/MnO_2 (Fig. 4d), the lower charge on Mn-centers close to Au implies a weaker EtOH coordination with respect to bare MnO_2 (d(Mn*−O_{Et}) = 2.02 Å), yielding a binding energy decrease (21.2 kcal/mol; Fig. S9† and Tables S3-S4†). Indeed, a weaker EtOH binding may favour its surface detachment once the EOR has taken place, aiding thus an easy catalyst regeneration. In addition, the ethanol molecule forms a short-strong hydrogen bond with Au/MnO_2 surface oxygen (d(O*−H) = 1.37 Å, Fig. 4d and S10†), an interface phenomenon that, *via* quantum delocalization effects, induces molecule-surface proton sharing and causes a substantial O-H bond

weakening.[44] Hence, interaction with the Au/MnO_2 surface leads to a pre- dissociation of ethanol, easing the subsequent EOR. Additionally, the DOS projected on EtOH O_{2p}-states (Fig. 4f) reveals that ethanol pre-oxidation also occurs. When EtOH is adsorbed on bare MnO_2, its O_{2p}-states remain partially occupied, as indicated by the high value of the spin-up component close to E_f (black curve, Fig. 4f). Yet, the spin-down component depletion in proximity of E_f (red curve, Fig. 4f) shows that the clean MnO_2 surface induces an incipient EtOH partial oxidation. This effect is greatly enhanced when EtOH is adsorbed on Au/MnO_2, as its O_{2p}-states are nearly empty for both spin components (green and blue curves, Fig. 4f). This finding indicates a more effective pre-oxidizing action of Au-decorated MnO_2 towards ethanol compared to bare MnO_2. Hence, the key contribution of Au to the catalytic performances of Au/MnO_2 is the creation of new, easily accessible low energy empty electronic states. In addition, the charge donation from Au atoms at the Au/MnO_2 interface favors the formation of a short-strong hydrogen bond in which EtOH shares its proton with a surface oxygen. Therefore, although Au atoms are not apparently directly bonded to EtOH, their catalytic role in the target process is indeed crucial. Altogether, the Au-induced electronic structure modifications explain the higher EOR efficiency of Au/MnO_2 *vs*. bare MnO_2 and shed light on its atomistic origin: upon adsorption on Au/MnO_2, ethanol undergoes partial oxidation and deprotonation, thus paving the way to EOR.

Conclusions

In summary, 3D hierarchical MnO_2-based architectures were grown on the surface of Ni foam by an innovative plasma-assisted fabrication strategy, involving the initial PA-CVD of MnO_2 in $Ar-O_2$ atmospheres, followed by functionalization with Au NPs by RF-sputtering from Ar plasmas. A combination of theory and experiments revealed the formation of phase-pure β-MnO_2 nanosystems, characterized by an intimate contact with low-sized Au NPs and offering at the same time a high active area in contact with the reaction medium. The developed systems yielded excellent functional performances as EOR electrocatalysts in alkaline environments. The positive Au NPs effect was due to a profound modification of the MnO_2 electronic structure, yielding $Au{\rightarrow} MnO_2$ charge donation and the formation of new low energy empty states. This causes a substantial weakening of the ethanol O-H bond, and a more effective oxidizing action towards ethanol. Overall, the presently reported findings not only afford a convenient preparative route to fabricate 3D nanoarchitectures with controllable phase composition, but also provide new atomistic insights into metal-oxide interactions and their key role in enhancing electrocatalytic performances. This knowledge, combined with the proposed fabrication route, may guide the development of electrocatalysts based on earth-abundant metal-oxides for ethanol valorization by electrical energy from renewable sources and for (photo)electrochemical water splitting.

Conflicts of interest

The authors declare no competing financial interests.

Acknowledgements

Notes and references

1. L. Zeng, K. Zhou, L. Yang, G. Du, L. Liu and W. Zhou, *ACS Appl. Energy Mater.*, 2018, **1**, 6279-6287.
2. S. Lian, M. P. Browne, C. Domínguez, S. N. Stamatin, H. Nolan, G. S. Duesberg, M. E. G. Lyons, E. Fonda and P. E. Colavita, *Sustain. Energy Fuels*, 2017, **1**, 780-788.
3. Y. T. Meng, W. Q. Song, H. Huang, Z. Ren, S. Y. Chen and S. L. Suib, *J. Am. Chem. Soc.*, 2014, **136**, 11452-11464.
4. N. K. Chaudhari, H. Jin, B. Kim and K. Lee, *Nanoscale*, 2017, **9**, 12231-12247.
5. S. Sun, Y. Zhou, B. Hu, Q. Zhang and Z. J. Xu, *J. Electrochem. Soc.*, 2016, **163**, H99-H104.
6. G. M. K. Tolba, N. A. M. Barakat, A. M. Bastaweesy, E. A. Ashour, W. Abdelmoez, M. H. El-Newehy, S. S. Al-Deyab and H. Y. Kim, *J. Mater. Sci. Technol.*, 2015, **31**, 97-105.
7. Z. Jia, Y. Wang and T. Qi, *RSC Adv.*, 2015, **5**, 83314-83319.
8. Q. Liu, K. Jiang, J. Fan, Y. Lin, Y. Min, Q. Xu and W.-B. Cai, *Electrochim. Acta*, 2016, **203**, 91-98.
9. A. De and J. Datta, *ACS Sustain. Chem. Eng.*, 2018, **6**, 13706-13718.
10. H. B. Hassan and R. H. Tammam, *Solid State Ionics*, 2018, **320**, 325-338.
11. J. Zhan, M. Cai, C. Zhang and C. Wang, *Electrochim. Acta*, 2015, **154**, 70-76.
12. A. Santasalo-Aarnio, E. Sairanen, R. M. Arán-Ais, M. C. Figueiredo, J. Hua, J. M. Feliu, J. Lehtonen, R. Karinen and T. Kallio, *J. Catal.*, 2014, **309**, 38-48.
13. H. B. Hassan, Z. A. Hamid and R. M. El-Sherif, *Chin. J. Catal.*, 2016, **37**, 616-627.
14. M. Nakayama, K. Suzuki and K. Fujii, *Electrochem. Commun.*, 2019, **105**, 106492.
15. A. Eshghi, E. Sadati Behbahani, M. Kheirmand and M. Ghaedi, *Int. J. Hydrogen Energy*, 2019, **44**, 28194-28205.
16. M. Tahir, L. Pan, F. Idrees, X. Zhang, L. Wang, J.-J. Zou and Z. L. Wang, *Nano Energy*, 2017, **37**, 136-157.
17. R. Frydendal, L. C. Seitz, D. Sokaras, T. C. Weng, D. Nordlund, I. Chorkendorff, I. E. L. Stephens and T. F. Jaramillo, *Electrochim. Acta*, 2017, **230**, 22-28.
18. S. Hernandez, C. Ottone, S. Varetti, M. Fontana, D. Pugliese, G. Saracco, B. Bonelli and M. Armandi, *Materials*, 2016, **9**, 296.
19. C. Xiao, S. Li, X. Zhang and D. R. MacFarlane, *J. Mater. Chem. A*, 2017, **5**, 7825-7832.
20. R. Adhikari, K. Basu, Y. Zhou, F. Vetrone, D. Ma, S. Sun, F. Vidal, H. Zhao and F. Rosei, *J. Mater. Chem. A*, 2018, **6**, 6822-6829.
21. R. Adhikari, L. Jin, F. Navarro-Pardo, D. Benetti, B. AlOtaibi, S. Vanka, H. Zhao, Z. Mi, A. Vomiero and F. Rosei, *Nano Energy*, 2016, **27**, 265-274.
22. D. Zhang, J. Zhang, H. Wang, C. Cui, W. Jiao, J. Gao and Y. Liu, *J. Alloys Compd.*, 2019, **806**, 1419-1429.
23. F. Kaedi, Z. Yavari, M. Asmaei, A. R. Abbasian and M. Noroozifar, *New J. Chem.*, 2019, **43**, 3884-3890.
24. L. Dai, Q. Qin, X. Zhao, C. Xu, C. Hu, S. Mo, Y. O. Wang, S. Lin, Z. Tang and N. Zheng, *ACS Cent. Sci.*, 2016, **2**, 538-544.
25. S. Sarkar, R. Jana, H. Vadlamani, S. Ramani, D. Mumbaraddi and S. C. Peter, *ACS Appl. Mater. Interfaces*, 2017, **9**, 15373-15382.
26. L. Karuppasamy, C. Y. Chen, S. Anandan and J. J. Wu, *Electrochim. Acta*, 2017, **246**, 75-88.
27. R. Frydendal, M. Busch, N. B. Halck, E. A. Paoli, P. Krtil, I. Chorkendorff and J. Rossmeisl, *ChemCatChem*, 2015, **7**, 149-154.
28. Y. Gorlin, C.-J. Chung, J. D. Benck, D. Nordlund, L. Seitz, T.-C. Weng, D. Sokaras, B. M. Clemens and T. F. Jaramillo, *J. Am. Chem. Soc.*, 2014, **136**, 4920-4926.
29. B. Liu, I. M. Mosa, W. Song, H. Zheng, C.-H. Kuo, J. F. Rusling, S. L. Suib and J. He, *J. Mater. Chem. A*, 2016, **4**, 6447-6455.
30. R. H. Tammam, A. M. Fekry and M. M. Saleh, *Int. J. Hydrogen Energy*, 2015, **40**, 275-283.
31. M. Fekete, R. K. Hocking, S. L. Y. Chang, C. Italiano, A. F. Patti, F. Arena and L. Spiccia, *Energy Environ. Sci.*, 2013, **6**, 2222-2232.
32. F. Mattelaer, T. Bosserez, J. Ronge, J. A. Martens, J. Dendooven and C. Detavernier, *RSC Adv.*, 2016, **6**, 98337-98343.
33. A. Ramírez, P. Hillebrand, D. Stellmach, M. M. May, P. Bogdanoff and S. Fiechter, *J. Phys. Chem. C*, 2014, **118**, 14073-14081.
34. C.-H. Kuo, W. Li, L. Pahalagedara, A. M. El-Sawy, D. Kriz, N. Genz, C. Guild, T. Ressler, S. L. Suib and J. He, *Angew. Chem. Int. Ed.*, 2015, **54**, 2345-2350.
35. F. Cheng, T. Zhang, Y. Zhang, J. Du, X. Han and J. Chen, *Angew. Chem. Int. Ed.*, 2013, **52**, 2474-2477.
36. R. Frydendal, E. A. Paoli, I. Chorkendorff, J. Rossmeisl and I. E. L. Stephens, *Adv. Energy Mater.*, 2015, **5**, 1500991.
37. T. Zhang, F. Cheng, J. Du, Y. Hu and J. Chen, *Adv. Energy Mater.*, 2015, **5**, 1400654.
38. G. Cheng, S. Xie, B. Lan, X. Zheng, F. Ye, M. Sun, X. Lu and L. Yu, *J. Mater. Chem. A*, 2016, **4**, 16462-16468.
39. Z. Yu, B. Duong, D. Abbitt and J. Thomas, *Adv. Mater.*, 2013, **25**, 3302-3306.
40. B. Jia, W. Chen, J. Luo, Z. Yang, L. Li and L. Guo, *Adv. Mater.*, 2020, **32**, 1906582.
41. J. Kang, A. Hirata, L. Kang, X. Zhang, Y. Hou, L. Chen, C. Li, T. Fujita, K. Akagi and M. Chen, *Angew. Chem. Int. Ed.*, 2013, **52**, 1664-1667.
42. Z. Xu, J. Yu and G. Liu, *Electrochem. Commun.*, 2011, **13**, 1260-1263.
43. L. Bigiani, D. Zappa, D. Barreca, A. Gasparotto, C. Sada, G. Tabacchi, E. Fois, E. Comini and C. Maccato, *ACS Appl. Mater. Interfaces*, 2019, **11**, 23962-23700.
44. G. Tabacchi, M. Fabbiani, L. Mino, G. Martra and E. Fois, *Angew. Chem. Int. Ed.*, 2019, **58**, 12431-12434.